

ARTICLE

DOI: 10.1038/s41467-018-06437-1

OPEN

# Stabilizing black phosphorus nanosheets via edge-selective bonding of sacrificial C<sub>60</sub> molecules

Xianjun Zhu<sup>1</sup>, Taiming Zhang<sup>2</sup>, Daochuan Jiang<sup>2</sup>, Hengli Duan<sup>3</sup>, Zijun Sun<sup>2</sup>, Mengmeng Zhang<sup>1</sup>, Hongchang Jin<sup>2</sup>, Runnan Guan<sup>1</sup>, Yajuan Liu<sup>1</sup>, Muqing Chen<sup>1</sup>, Hengxing Ji<sup>2</sup>, Pingwu Du<sup>2</sup>, Wensheng Yan<sup>3</sup>, Shiqiang Wei<sup>3</sup>, Yalin Lu<sup>1</sup> & Shangfeng Yang<sup>1</sup>

Few-layer black phosphorus (BP) with an anisotropic two-dimensional (2D)-layered structure shows potential applications in photoelectric conversion and photocatalysis, but is easily oxidized under ambient condition preferentially at its edge sites. Improving the ambient stability of BP nanosheets has been fulfilled by chemical functionalization, however this functionalization is typically non-selective. Here we show that edge-selective functionalization of BP nanosheets by covalently bonding stable C<sub>60</sub> molecules leads to its significant stability improvement. Owing to the high stability of the hydrophobic C<sub>60</sub> molecule, C<sub>60</sub> functions as a sacrificial shield and effectively protects BP nanosheets from oxidation under ambient condition. C<sub>60</sub> bonding leads to a rapid photoinduced electron transfer from BP to C<sub>60</sub>, affording enhanced photoelectrochemical and photocatalytic activities. The selective passivation of the reactive edge sites of BP nanosheets by sacrificial C<sub>60</sub> molecules paves the way toward ambient processing and applications of BP.

<sup>1</sup>Hefei National Laboratory for Physical Sciences at Microscale, CAS Key Laboratory of Materials for Energy Conversion, Department of Materials Science and Engineering, Synergetic Innovation Center of Quantum Information & Quantum Physics, University of Science and Technology of China, Hefei 230026, China.

<sup>2</sup>CAS Key Laboratory of Materials for Energy Conversion, iChEM (Collaborative Innovation Center of Chemistry for Energy Materials), Department of Materials Science and Engineering, University of Science and Technology of China, Hefei 230026, China. <sup>3</sup>National Synchrotron Radiation Laboratory, University of Science and Technology of China, Hefei 230029, China. Correspondence and requests for materials should be addressed to S.Y. (email: [sfyang@ustc.edu.cn](mailto:sfyang@ustc.edu.cn))

Few-layer black phosphorus (BP), a two-dimensional (2D)-layered semiconductor that can be exfoliated from bulk BP, has been attracting increasing interest owing to its unique band structure featuring direct band gap with thickness-dependent gap energy in the range of 0.3–2.0 eV and high charge carrier mobility of  $\sim 1000 \text{ cm}^2 \text{ V}^{-1} \text{ s}^{-1}$ , rendering its potential applications in transistors, biomedicine, energy conversion, and storage<sup>1–6</sup>. Realization of such applications of few-layer BP is largely dependent on exfoliated BP nanosheets, which are however easily oxidized under ambient condition because each phosphorus atom has a pair of lone electrons prone to react with oxygen adsorbed on the surface of BP nanosheets<sup>7–10</sup>. The oxidation rate of BP nanosheets was found by Favron et al. to depend linearly on oxygen concentration dissolved in adsorbed water and light intensity<sup>8</sup>. A more recent report by Kuntz et al. revealed that pure oxygen led to oxidation of the van der Waals surface of BP, whereas water oxidized BP at pre-existing defects such as edges or steps<sup>10</sup>. Thus, improving the ambient stability of BP is a prerequisite for its practical applications<sup>11</sup>. So far several strategies have been developed to improve the ambient stability of BP nanosheets, which includes, for instance, protective layers coating<sup>12,13</sup>, heteroatoms doping<sup>14</sup>, and hybridization with other chemicals<sup>15–18</sup> and chemical functionalization<sup>19,20</sup>. Among them, chemical functionalization has been implemented as one of the most effective routes to passivate the reactive BP, fulfilled by either covalent functionalization<sup>19</sup>, coordination<sup>20</sup>, or non-covalent functionalization via van der Waals (vdW) heterostructure formation or electrostatic interactions<sup>21–23</sup>. Noteworthy, these reported chemical functionalization approaches are typically non-selective, mostly on the surface of BP nanosheets<sup>19–23</sup>. Although surface functionalization can effectively passivate the phosphorus atoms located on the puckered surface, the involvement of functional groups can result in strong structure perturbation, consequently compromising the unique electronic structures of BP. Such an influence is amplified in few-layer BP nanosheets due to its improved specific surface area. On the other hand, P atoms at the edge sites are found to be more reactive in oxidation than those at the surface of phosphorene<sup>10</sup>. Thus, selective functionalization of BP, especially at its edges, is highly desired for passivating BP without losing its surface integrity. However, edge-selective functionalization of BP nanosheets has rarely been reported because of the difficulty in selectively activating its edge sites and finding a functional molecule with suitable reactivity which affords reaction with the more reactive edge sites only.

Fullerenes such as  $\text{C}_{60}$  as the first member of nanocarbon family are one of the most representative molecular materials, showing high stability against light, oxygen and water due to its hydrophobicity and spherical aromaticity<sup>24–28</sup>. These features along with its strong electron-accepting ability render the potential applications of fullerenes in versatile fields including energy conversion, catalysis, biomedicines<sup>29–31</sup>. Given that the low ambient stability of BP nanosheets is primarily due to its facile oxidation under the conditions of light, oxygen and water<sup>7–10</sup>, an intriguing idea is whether incorporating stable  $\text{C}_{60}$  molecules would prevent BP from oxidation. Besides, compared to such small molecules as aryl diazonium which afforded surface functionalization of BP<sup>19</sup>, the lower reactivity of  $\text{C}_{60}$  may benefit edge-selective functionalization of BP nanosheets. Nevertheless, to the best of our knowledge, up to now hybrid of BP and  $\text{C}_{60}$  has been scarcely reported primarily due to the difficulty on hybridization owing to their divergence on the dimensions.

Herein, we report the edge-selective bonding of  $\text{C}_{60}$  molecules onto BP nanosheets via covalent phosphorus–carbon bonds, accomplished via a facile one-step solid-state mechanochemical route by ball-milling bulk BP and  $\text{C}_{60}$  powders without any

additive. On the basis of a series of morphological and spectroscopic characterizations, the successful edge-selective bonding of  $\text{C}_{60}$  within BP- $\text{C}_{60}$  hybrid was confirmed. The effect of  $\text{C}_{60}$  bonding on the stability of BP nanosheets in water is studied.  $\text{C}_{60}$  molecules bonding at the edges of BP nanosheets serve as sacrificial shield, resulting in significant stability improvement of BP nanosheets against oxidation as well as obviously enhanced photoelectrochemical and photocatalytic activities of BP. Thus, our strategy on selectively passivating the reactive edge sites of BP nanosheets by sacrificial  $\text{C}_{60}$  molecules opens up new avenues for versatile applications of BP.

## Results

**Synthesis and characterization of the BP- $\text{C}_{60}$  hybrid.** As an alternative route to the solution-phase chemical functionalization, solid-state mechanochemical method has recently been extensively applied to prepare edge-selectively functionalized graphene nanosheets by attaching different elements, small inorganic molecules or  $\text{C}_{60}$ <sup>32–34</sup>. Given that BP has a 2D-layered structure analogous to graphene, we are stimulated to employ solid-state mechanochemical method to synthesize BP nanosheets with edge-selectively bonded  $\text{C}_{60}$  based on its simplicity and environmental-friendliness (without using any organic solvent). Three hundred milligrams of bulk BP, which was prepared by a phase transformation reaction from red phosphorus<sup>35</sup>, and 600 mg  $\text{C}_{60}$  powder were mixed and ball-milled directly under an Ar atmosphere in a planetary ball-milling machine (Fig. 1a). After ball-milling at 250 rpm for 24 h, the resultant black mixture was collected and Soxhlet-extracted with  $\text{CS}_2$  for 48 h to remove the unreacted  $\text{C}_{60}$ . Note that, previously Cui et al. made an attempt to synthesize a BP- $\text{C}_{60}$  composite via mechanochemical ball-milling route as a comparative study with BP-graphite composite synthesized under the same condition. However, in their report carbon materials including graphite and  $\text{C}_{60}$  were ball-milled prior to blending with BP, thus a two-step ball-milling process was needed for synthesizing their BP- $\text{C}_{60}$  composite. Besides, whether or not  $\text{C}_{60}$  molecules bonded directly with BP remained unclear<sup>15</sup>. Hence, in our present study, we managed to simplify the process to one-step and unravel clearly how  $\text{C}_{60}$  molecules bond with BP.

Scanning electron microscopy (SEM) was carried out to study the morphology of BP- $\text{C}_{60}$  hybrid. Compared to the bulk BP which shows large sheets with sizes of more than  $10 \mu\text{m}$  (Supplementary Fig. 1a), BP- $\text{C}_{60}$  hybrid exhibits aggregated particles with sizes of  $\sim 1 \mu\text{m}$  in average (Supplementary Fig. 1b). For comparison, we also prepared two control samples obtained by ball-milling BP with LiOH as additive (abbreviated as BP-BM)<sup>6</sup> and ball-milling  $\text{C}_{60}$  only (abbreviated as  $\text{C}_{60}$ -BM) under the same ball-milling condition, and found that BP-BM shows smaller aggregated particles (Supplementary Fig. 1c) compared to that of BP- $\text{C}_{60}$  hybrid. This is understandable since the existence of  $\text{C}_{60}$  would dissipate the mechanical energy of ball-milling effective for cleaving BP sheets. The average thickness of BP- $\text{C}_{60}$  hybrid, acquired by atomic force microscopic (AFM) analyses (Supplementary Fig. 2), is  $\sim 2.5 \text{ nm}$ , which is comparable to that of BP-BM ( $\sim 2.7 \text{ nm}$ ) and corresponds to  $\sim 4$ -layer nanosheets based on the interlayer distance of  $\sim 0.52 \text{ nm}$  (ref. 2). An average  $\text{C}_{60}$  molar content of 19 per 1000 P atoms was estimated according to the weight ratio of  $\text{C}_{60}$  ( $\sim 30\%$ ) within the BP- $\text{C}_{60}$  hybrid determined by thermogravimetric analysis (TGA) (Supplementary Fig. 3). The X-ray diffraction (XRD) pattern of BP- $\text{C}_{60}$  hybrid shows intensive peaks at  $16.8^\circ$ ,  $34.2^\circ$ , and  $52.3^\circ$ , which are indexed as the (020), (040), and (060) planes of BP, respectively (Supplementary Fig. 4), thus the crystal structure of BP is preserved after ball-milling. Besides, the signals of  $\text{C}_{60}$  crystals are

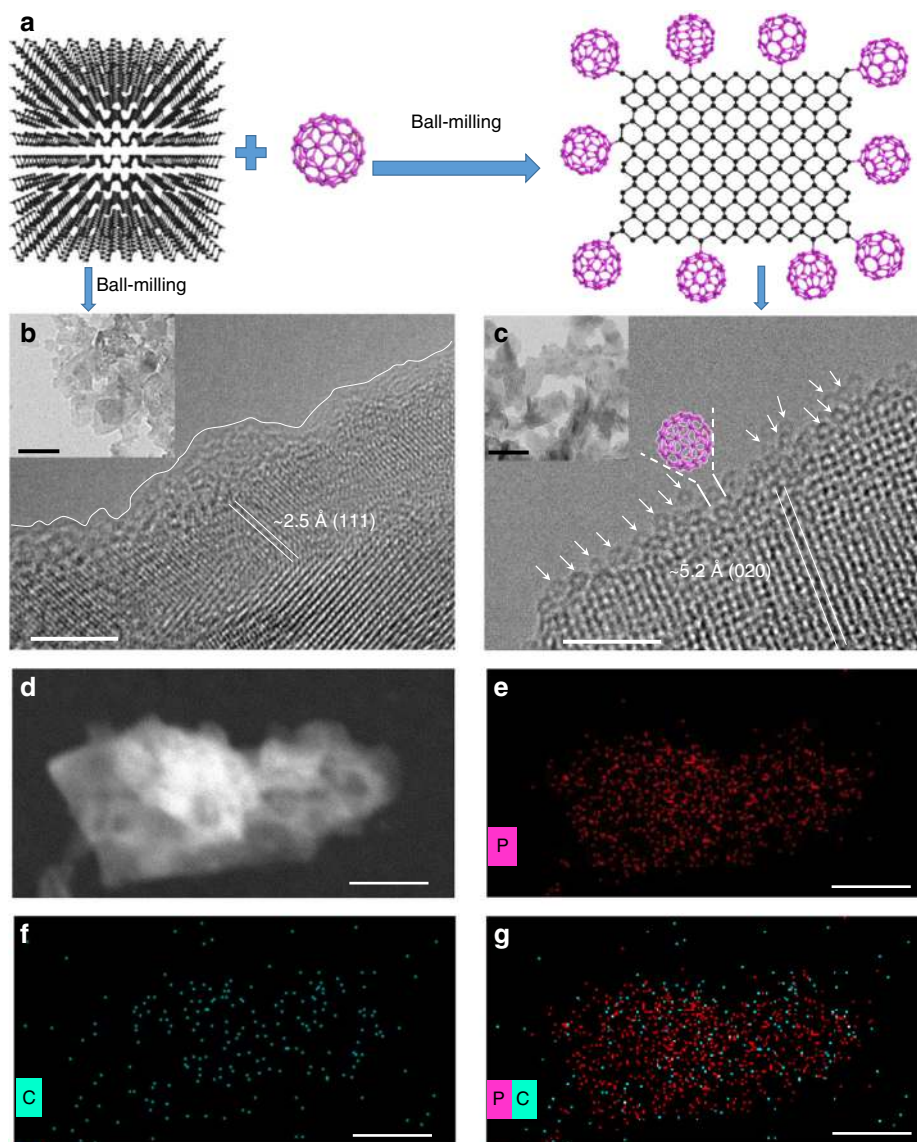


**Fig. 1** Microstructural characterizations. **a** Scheme of the preparation process and structure of BP-C<sub>60</sub> hybrid. **b** HRTEM and low-magnification TEM (inset, scale bar: 100 nm) images of ball-milled BP (BP-BM). Inset: **c** HRTEM and low-magnification TEM (inset, scale bar: 100 nm) images of the BP-C<sub>60</sub> hybrid. The arrows mark the C<sub>60</sub> molecules. **d-g** STEM and EDX elemental (P and C) mapping images of the BP-C<sub>60</sub> hybrid. The scale bars are 5, 5, 100, 100, 100, and 100 nm in **b**, **c**, **d**, **e**, **f**, and **g**, respectively

invisible in the XRD pattern of BP-C<sub>60</sub> hybrid, indicating the complete removal of unreacted C<sub>60</sub> by Soxhlet-extraction.

The transmission electron microscopy (TEM) image of BP-BM shows flat nanosheets (inset of Fig. 1b, see also Supplementary Fig. 5b for a large-area image). According to the high-resolution TEM (HRTEM) image, the lattice fringes of (111) plane with space distance of  $\sim 2.5$  Å were observed at the edge of BP nanosheets, which is covered with amorphous coating due to the existence of defects resulted from P atom reconstruction at the edges of BP nanosheets during ball-milling process as well as the attachment of the hydroxyl groups at the edges introduced by LiOH additive (Fig. 1b). The amorphous coating may raise from oxidation of BP since the specimen had to be exposed in air for hours before transferred into TEM chamber. In contrast, the TEM image of the BP-C<sub>60</sub> hybrid shows lattice fringes of (020) plane at the edges of the BP nanosheets without amorphous coating (Fig. 1c), even though the BP-C<sub>60</sub> sample was exposed in air together with BP-BM, indicating that the BP-C<sub>60</sub> hybrid has an improved structure stability at ambient condition.

Interestingly, along the edges of the BP nanosheets, hollow nanospheres with diameter of  $\sim 1.0$  nm are observed in the high-resolution TEM (HRTEM) image of the BP-C<sub>60</sub> hybrid (Fig. 1c), which match well with the morphology of C<sub>60</sub> molecules with a van der Waals diameter of  $\sim 1.0$  nm<sup>24,25</sup>. These results indicate that C<sub>60</sub> molecules primarily attach at the edges of BP nanosheets. Moreover, we carried out scanning transmission electron microscopy-energy dispersive X-ray spectroscopic (STEM-EDX) measurements to study the chemical distribution of the BP-C<sub>60</sub> hybrid, and found that the P elements distribute homogeneously over the entire nanosheet whereas C elements have a much lower content than P elements (Fig. 1d-g). Thus, C<sub>60</sub> bonding onto the surface of BP nanosheets can be excluded otherwise a much higher content of C elements should have been observed.

It is intriguing to determine whether C<sub>60</sub> molecules attach onto the edges of BP nanosheets via covalent bonding or physical adsorption. We performed a series of spectroscopic characterizations to address this issue. For comparison, we prepared a physical mixture of BP-BM and C<sub>60</sub> (abbreviated as BP/C<sub>60</sub>

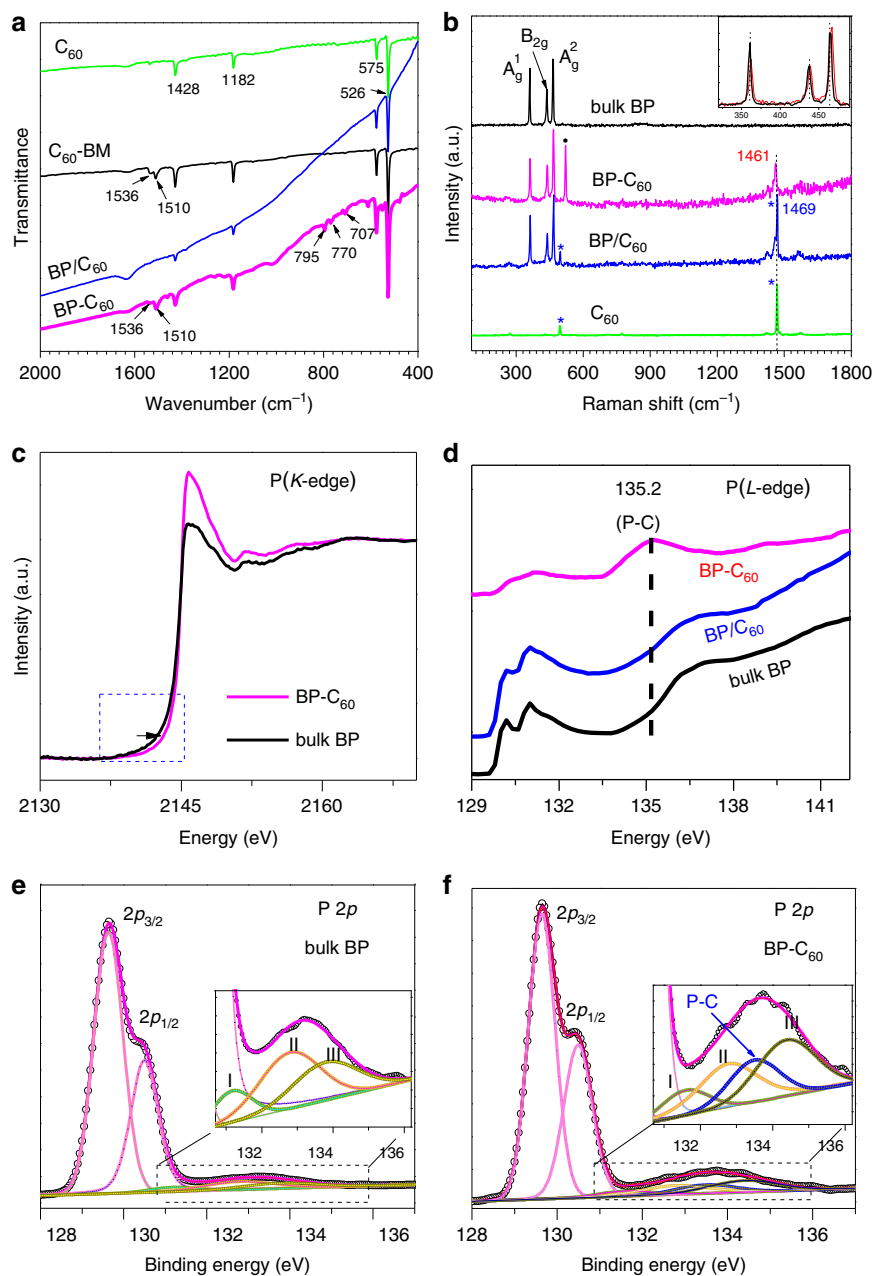


**Fig. 2** Spectroscopic characterizations. **a** FTIR spectra of the pristine  $C_{60}$ ,  $C_{60}$ -BM, BP/ $C_{60}$  mixture and the BP- $C_{60}$  hybrid. **b** Raman spectra of bulk BP, the BP- $C_{60}$  hybrid, BP/ $C_{60}$  mixture, and pristine  $C_{60}$ . The filled circle marks the signal of Si substrate, and the asterisks label the signal of  $C_{60}$ . Inset: enlarged spectra of bulk BP and the BP- $C_{60}$  hybrid. **c** P K-edge XAS spectra of bulk BP and the BP- $C_{60}$  hybrid. **d** P L-edge XAS spectra of bulk BP, BP/ $C_{60}$  mixture and the BP- $C_{60}$  hybrid. **e** High-resolution P2p XPS spectra of bulk BP. **f** High-resolution P2p XPS spectra of the BP- $C_{60}$  hybrid. Numbers I-III label the signals assigned to P-O-P (bridging bonding), O-P=O (dangling bonding), and  $P_2O_5$ , respectively<sup>6</sup>

mixture, in which the weight ratio of  $C_{60}$  is  $\sim 30\%$ , close to that within BP- $C_{60}$  hybrid) as a control sample. We first performed Fourier-transform infrared (FTIR) and solid-state  $^{13}C$  and  $^{31}P$  nuclear magnetic resonance (NMR) spectroscopic studies so as to investigate the bonding structure of  $C_{60}$  in the BP- $C_{60}$  hybrid. The FTIR spectrum of the BP- $C_{60}$  hybrid (Fig. 2a) shows four characteristic vibrational peaks of  $C_{60}$  at 526, 576, 1182, and 1428  $cm^{-1}$  without appreciable shift relative to the pristine  $C_{60}$ , indicating the existence of  $C_{60}$  moiety in the BP- $C_{60}$  hybrid (see also Supplementary Fig. 6 for comparison with bulk BP and BP-BM). Besides, several new vibrational peaks at 707, 770, 795, 1510, and 1536  $cm^{-1}$  appear in the spectrum of the BP- $C_{60}$  hybrid. Except the vibrational peaks at 1510 and 1536  $cm^{-1}$

which are also detected in the spectrum of  $C_{60}$ -BM, the three new vibrational peaks at 707, 770, and 795  $cm^{-1}$  are exclusively observed in the spectrum of the BP- $C_{60}$  hybrid but absent in that of BP/ $C_{60}$  mixture. These results confirm that the BP- $C_{60}$  hybrid is not a physical mixture of BP-BM, and the new vibrational peaks should originate from the as-formed phosphorus-carbon (P-C) covalent bonds<sup>15,36</sup>. In the solid-state  $^{13}C$ -NMR spectrum of BP- $C_{60}$  hybrid, intense signals in the region of 130–160 ppm are detected, which are typical for  $sp^2$ -carbon of  $C_{60}$ , and an additional weak peak at 75.75 ppm is observed, which is absent in the spectra of both BP/ $C_{60}$  mixture and pure  $C_{60}$  (Supplementary Fig. 7), confirming the formation of  $sp^3$ -carbon on the  $C_{60}$  cage. On the other hand, according to the comparison of the solid-state



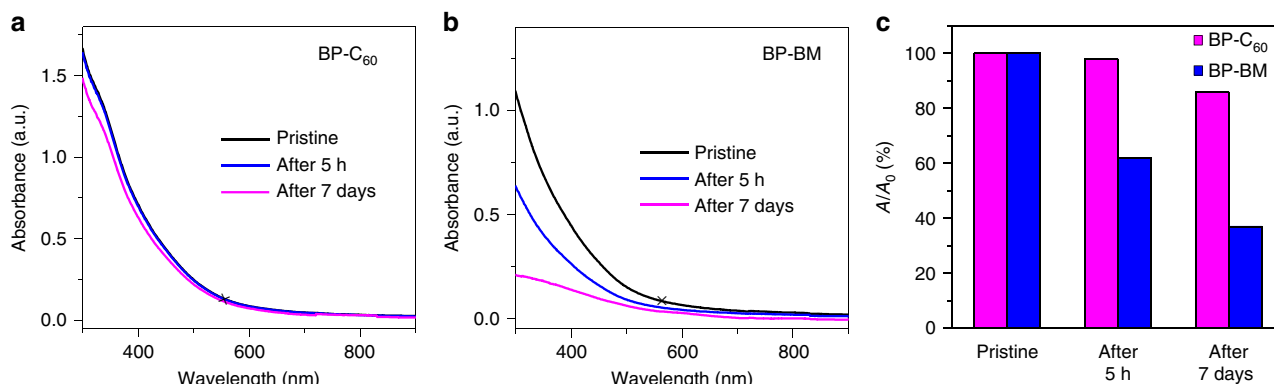


**Fig. 3** Stabilities of the BP- $C_{60}$  hybrid and BP-BM dispersions in water. UV-vis absorption spectra of the BP- $C_{60}$  hybrid (a) and BP-BM (b) dispersed in water after standing for different times. c Variation of the absorption ratios ( $A/A_0$ ) at 550 nm (marked by a cross) of BP- $C_{60}$  and BP-BM dispersions with different times

$^{31}\text{P}$  NMR spectra of the BP- $C_{60}$  hybrid, bulk BP and BP/ $C_{60}$  mixture, the intense signal at 21.68 ppm observed in bulk BP is obviously broadened with the appearance of several shoulder peaks in the high field in the spectra of both the BP- $C_{60}$  hybrid and BP/ $C_{60}$  mixture probably due to the decreased crystallinity and the covalent functionalization of BP caused by ball-milling<sup>6,37</sup>. Interestingly, the signal peak at 21.68 ppm observed in bulk BP shifts to 22.86 ppm in the spectrum of the BP- $C_{60}$  hybrid (Supplementary Fig. 7), suggesting a deshielding effect with decrease of electron density of the nucleus of P atom. On the contrary, for BP/ $C_{60}$ -mixture such a signal peak negatively shifts to 19.62 ppm due to the covalent bonding of the hydroxyl functional groups<sup>6</sup>. The dramatic difference between the spectra of the BP- $C_{60}$  hybrid and BP/ $C_{60}$ -mixture solidifies the conclusion that the BP- $C_{60}$  hybrid is not the physical mixture of BP and  $C_{60}$ .

Figure 2b compares Raman spectra of the BP- $C_{60}$  hybrid, bulk BP, pristine  $C_{60}$ , and BP/ $C_{60}$  mixture. Bulk BP exhibits three intense Raman signals at 361, 437, and 465  $\text{cm}^{-1}$ , which are assigned to  $A_g^1$ ,  $B_{2g}$  and  $A_g^2$  modes, respectively<sup>38</sup>. In the Raman spectrum of pristine  $C_{60}$ , two intense signals are observed at 495 and 1469  $\text{cm}^{-1}$  corresponding to  $A_g^1$  and  $A_g^2$  mode, respectively<sup>39</sup>. For the BP/ $C_{60}$  mixture, its Raman spectrum shows a superposition of signals of BP and  $C_{60}$  moieties without any shifts, indicating no strong intermolecular interactions between BP and  $C_{60}$  moieties. Instead, the Raman spectrum of the BP- $C_{60}$  hybrid is apparently different from that of BP/ $C_{60}$ -mixture in terms of the absence of the signal at 495  $\text{cm}^{-1}$  ( $A_g^1$  mode) and the down-shift of the most intense  $A_g^2$  mode (1469  $\text{cm}^{-1}$ ) of pristine  $C_{60}$  by  $\sim 8$  to 1461  $\text{cm}^{-1}$ . Since the latter peak ( $A_g^2$  mode) is sensitive to the charge state of  $C_{60}$ , such a down-shift suggests that charge transfer from BP to  $C_{60}$  may take place due to the well-known strong electron-accepting ability of  $C_{60}$ <sup>24,34</sup>. These results indicate that the BP- $C_{60}$  hybrid is not a physical mixture of BP-BM and  $C_{60}$  otherwise charge transfer from BP to  $C_{60}$  could not have happened, instead  $C_{60}$  molecules attach onto the edges of BP nanosheets via covalent bonding. Besides, the three characteristic Raman peaks of bulk BP show negligible shifts and relative intensity change in the spectrum of the BP- $C_{60}$  hybrid (see inset of Fig. 2b), confirming that  $C_{60}$  molecules primarily attach at the edges of BP nanosheets otherwise obvious change of their relative intensity would have been visible if surface grafting of  $C_{60}$  molecules onto BP nanosheets occurred<sup>19</sup>.

To further analyze the bonding structure of BP in the BP- $C_{60}$  hybrid, we carried out X-ray absorption spectroscopic (XAS) and X-ray photoemission spectroscopic (XPS) studies. P  $K$ -edge XAS

spectra of the BP- $C_{60}$  hybrid and bulk BP are compared in Fig. 2c. The XAS spectrum of the BP- $C_{60}$  hybrid exhibits a more intense peak at 2145.8 eV and a blue-shift by  $\sim 1$  eV of the absorption edge compared to that of bulk BP, indicating the electron transfer from BP to  $C_{60}$ <sup>40,41</sup>. We further collected P  $L$ -edge XAS spectra of the BP- $C_{60}$  hybrid and bulk BP, which provide richer spectral features than the  $K$ -edge spectra<sup>42</sup>. As shown in Fig. 2d, the P  $L$ -edge XAS spectrum of bulk BP exhibits near-edge absorption peaks in the region of 129.5–132.5 eV corresponding to the P ( $2p$ )  $\rightarrow 1e^*$  transition and a broad peak at around 137.0 eV ascribed to transitions from  $2p_{3/2}$  and  $2p_{1/2}$  levels<sup>43,44</sup>. However, in the P  $L$ -edge XAS spectrum of the BP- $C_{60}$  hybrid, a new peak centered at  $\sim 135.2$  eV appears, which can be assigned to the as-formed P-C bonds<sup>8,38</sup>. Noteworthy, this peak is absent in the P  $L$ -edge XAS spectrum of the BP/ $C_{60}$  mixture, confirming further that the BP- $C_{60}$  hybrid is not a physical mixture of BP-BM and  $C_{60}$ .

Figure 2e, f compares the high-resolution P  $2p$  spectra of the BP- $C_{60}$  hybrid and bulk BP. In the high-resolution P  $2p$  XPS spectrum of bulk BP, two intense peaks centered at 129.6 and 130.5 eV are attributed to  $2p_{3/2}$  and  $2p_{1/2}$  of P-P bonds, while a weak broad peak at  $\sim 133.0$  eV is due to the unavoidable oxidation of BP (Fig. 2e)<sup>6,8,45–47</sup>. For the BP- $C_{60}$  hybrid, although the overall P  $2p$  XPS spectrum looks quite similar (Supplementary Fig. 8), a detailed deconvolution analysis reveals the appearance of a new peak centered at  $\sim 133.5$  eV, which can be assigned to P-C covalent bonds (Fig. 2f)<sup>19</sup>.

**Formation mechanism of the BP- $C_{60}$  hybrid.** Based on the aforementioned characterizations, we propose a plausible conformation of the BP- $C_{60}$  hybrid as well as its formation mechanism as illustrated in Supplementary Fig. 9. Similar to the studies of mechanochemical functionalization of graphene extensively reported in the literatures<sup>32–34</sup>, high-energy ball-milling of bulk BP results in its exfoliation to few-layer BP nanosheets along with the generation of the reactive species (radicals and ions) at the edges via a mechanochemical cleavage of P-P bonds. Simultaneously,  $C_{60}$  is activated by high-energy ball-milling<sup>33</sup>, and consequently attaches onto the activated edges of BP nanosheets via the covalent P-C bonds. In this sense, the attachment of  $C_{60}$  onto the surface of BP nanosheets is less preferable because the average thickness of the BP- $C_{60}$  hybrid ( $2.5 \pm 0.2$  nm) is even slightly smaller than that of BP-BM ( $2.7 \pm 0.2$  nm) according to AFM analyses (Supplementary Fig. 2). Thus, bonding of  $C_{60}$  onto BP nanosheets is highly edge-selective. Noteworthy, such an edge-selective bonding of  $C_{60}$  onto BP

nanosheets can be accomplished by blending bulk BP and  $C_{60}$  directly without any additive, thus being very facile and eco-friendly. In addition, we also carried out a control experiment with an attempt to improve the yield of the BP- $C_{60}$  hybrid by ball-milling the mixture of bulk BP and  $C_{60}$  in the existence of LiOH, which was a crucial additive for the formation of graphene- $C_{60}$  hybrid as reported previously<sup>34</sup>, but surprisingly found almost no hybrid formation according to Raman spectroscopic analysis (Supplementary Fig. 10).

**Ambient stability of the BP- $C_{60}$  hybrid.** It is well known that BP nanosheets can be easily oxidized under ambient condition, and previous reports reveal that surface functionalization of BP can effectively passivate the P atoms located on the puckered surface and consequently stabilize BP nanosheets<sup>19,20</sup>. It is thus stimulating to investigate whether the edge-selective functionalization by  $C_{60}$  can stabilize BP nanosheets as well. We monitored the optical absorbances of BP- $C_{60}$  hybrid and BP-BM which are both dispersed in water under ambient condition<sup>20</sup>. In the UV-vis absorption spectrum of the BP- $C_{60}$  hybrid dispersion, a shoulder peak at  $\sim 340$  nm appears (Fig. 3a), which is absent in the spectrum of BP-BM dispersion (Fig. 3b), confirming the existence of  $C_{60}$  moiety within the BP- $C_{60}$  hybrid (Supplementary Fig. 11). Noteworthy, the UV-vis absorbance of BP- $C_{60}$  dispersion at 550 nm shows only a slight decrease (by  $\sim 2\%$ ) after standing for 5 h, whereas there is a  $\sim 38\%$  decrease in the absorbance for BP-BM dispersion. After 7 days, the

absorbance of BP- $C_{60}$  dispersion retains at  $\sim 86\%$ , which is much larger than that of BP-BM dispersion ( $\sim 36\%$ , Fig. 3c). Therefore, the degradation rate of BP- $C_{60}$  in water is significantly inhibited by a factor of 4.6 compared to that of BP-BM. The significant improvement of the stability of the BP- $C_{60}$  hybrid is attributed to the bonding of stable  $C_{60}$  molecules via the covalent P-C bonds as confirmed by the above spectroscopic studies. Since  $C_{60}$  molecules have high stability against light, oxygen, and water<sup>24–27</sup>, bonding of  $C_{60}$  onto the edges of BP nanosheets provides a sacrificial shield which effectively prevents BP from attacks of light, oxygen and water (see Supplementary Fig. 9)<sup>10</sup>. Thus, we demonstrate that edge-selective functionalization by  $C_{60}$  can stabilize BP nanosheets other than surface functionalization.

**Photoelectrochemical and photocatalytic activities.** Upon improving the stability of BP nanosheets in water via edge-selective bonding of  $C_{60}$ , we next applied the BP- $C_{60}$  hybrid in photoelectrochemical cell and photocatalytic dye degradation. Figure 4a shows a typical photocurrent response curve of a photoelectrochemical cell composed of a BP- $C_{60}$  hybrid-modified FTO transparent electrode measured at a bias voltage of 0.2 V. Clearly, a photocurrent switching during light on-off cycles is observed, and the net photocurrent induced by the initial light illumination is  $\sim 1.2 \mu\text{A cm}^{-2}$ , which attenuates rapidly during the light illumination of 100 s (Fig. 4a). Such a photocurrent overshooting phenomenon upon light illumination has been often reported for

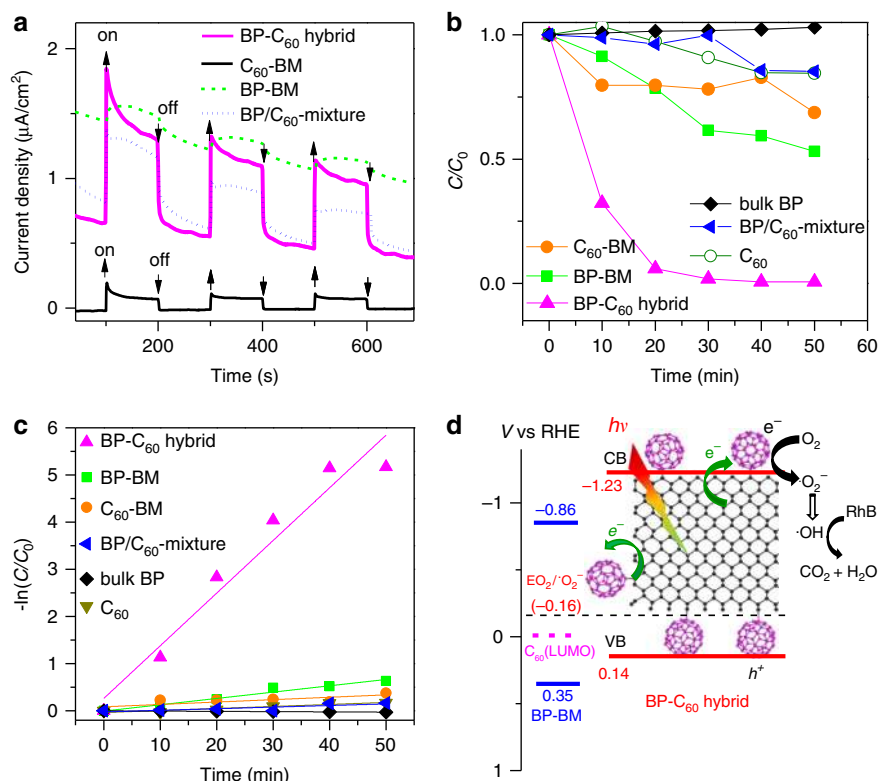


**Fig. 4** Photocurrent response and photocatalytic activities. **a** Photocurrent-time dependences of the BP- $C_{60}$  hybrid, BP/ $C_{60}$  mixture, BP-BM, and  $C_{60}$ -BM. For bulk BP, no photocurrent response was detected since the VB level of bulk BP ( $-0.01$  V vs RHE)<sup>6</sup> is even more negative than the work function of FTO, leading to a facile recombination of the photogenerated electron-hole pairs. **b** Photocatalytic degradation of RhB over the BP- $C_{60}$  hybrid, BP/ $C_{60}$  mixture, BP-BM,  $C_{60}$ -BM, pristine  $C_{60}$  and bulk BP powders under visible light.  $C$  and  $C_0$  denote the reaction and absorption equilibrium concentrations of RhB in the system. **c** Pseudo-first-order kinetics curves of RhB degradation over different samples. **d** The experimentally determined energy levels of the BP- $C_{60}$  hybrid and BP-BM, and a schematic illustration showing the mechanism of the photocatalytic dye degradation of the BP- $C_{60}$  hybrid. The lowest unoccupied molecular orbital (LUMO) energy level of  $C_{60}$  is also shown for comparison (see caption of Supplementary Fig. 13 for details)

photoelectrochemical cells based on semiconducting inorganic nanostructures, and is presumably due to the back electron transfer process<sup>48</sup>. For comparison, we also measured the photocurrent responses of BP-BM and C<sub>60</sub>-BM under the identical conditions. BP-BM exhibits a photocurrent response of  $\sim 0.12 \mu\text{A cm}^{-2}$ , which is comparable to that of BP nanosheets with comparable thickness reported in ref. <sup>49</sup>. The photocurrent of the BP-C<sub>60</sub> hybrid is around 10 times of that of BP-BM and also much higher than that of C<sub>60</sub>-BM ( $\sim 0.20 \mu\text{A cm}^{-2}$ ), indicating that the hybrid conformation is advantageous for enhancing the photoelectric conversion properties of both BP and C<sub>60</sub>. Compared to BP/C<sub>60</sub> mixture for which a photocurrent response of  $\sim 0.57 \mu\text{A cm}^{-2}$  is obtained, the photocurrent response of the BP-C<sub>60</sub> hybrid is around two times higher. This indicates again that BP-C<sub>60</sub> hybrid and BP/C<sub>60</sub> mixture are quite different, and the covalent bonding of C<sub>60</sub> onto BP is crucial for improving the photocurrent response. Since the optical absorption edge of the BP-C<sub>60</sub> hybrid is comparable to that of BP-BM (Supplementary Fig. 12a), the enhanced photoelectric conversion property can be attributed to the photoinduced electron transfer from BP to C<sub>60</sub> within the BP-C<sub>60</sub> hybrid as revealed by steady-state photoluminescence (PL) spectroscopic study (Supplementary Fig. 13a), which takes place in the order of tens to hundreds of picoseconds according to time-resolved photoluminescence (TRPL) spectroscopic result (Supplementary Fig. 13b).

We further evaluated the effect of C<sub>60</sub> bonding on the photocatalytic activity of BP for degradation of Rhodamine B (RhB) dye under visible light. Figure 4b compares the photocatalytic activities of the BP-C<sub>60</sub> hybrid, BP/C<sub>60</sub> mixture, bulk BP, pristine C<sub>60</sub>, BP-BM, and C<sub>60</sub>-BM. While bulk BP, pristine C<sub>60</sub>, BP-BM, C<sub>60</sub>-BM, and BP/C<sub>60</sub> mixture all show low photocatalytic activity, the BP-C<sub>60</sub> hybrid exhibits significantly enhanced photocatalytic activity with an apparent reaction rate constant ( $k$ ) of  $6.70 \text{ h}^{-1}$  based on fitting to a pseudo-first-order kinetics (Fig. 4b, c)<sup>50</sup>. Noteworthy, the photocatalytic activity of BP/C<sub>60</sub> mixture is much lower than that of the BP-C<sub>60</sub> hybrid, and is even lower than that of BP-BM due mainly to the decrease of the content of BP-BM ( $\sim 70 \text{ wt}\%$ ). This result reveals the advantage of the BP-C<sub>60</sub> hybrid formation in enhancing the photocatalytic activity of BP. To evaluate the stability of the BP-C<sub>60</sub> hybrid during photocatalytic degradation reactions, we measured the TEM image and P 2p XPS spectrum of the BP-C<sub>60</sub> hybrid after photocatalytic degradation reactions (Supplementary Figs. 14, 15), and found that the BP-C<sub>60</sub> hybrid kept the original form of nanosheets with comparable sizes to the original one, and no obvious oxidation occurred. Thus, the high stability of the BP-C<sub>60</sub> hybrid against oxidation during the photocatalytic degradation reactions is confirmed.

To unravel the mechanism responsible for the enhanced photocatalytic activity of the BP-C<sub>60</sub> hybrid, we measured its conduction band (CB) and valence band (VB) energy levels by synchrotron radiation photoemission spectroscopy (SR-PES), which are  $-3.27$  and  $-4.64 \text{ eV}$  versus vacuum level ( $-1.23$  and  $0.14 \text{ V}$  vs reversible hydrogen electrode (RHE)), respectively (Supplementary Figs. 16, 17 and Supplementary Table 1). Compared to BP-BM with CB/VB levels of  $-0.86/0.35 \text{ V}$  vs RHE, both of the CB and VB levels of the BP-C<sub>60</sub> hybrid shift negatively. In particular, the more negative CB level of the BP-C<sub>60</sub> hybrid facilitates the reduction of the dissolved O<sub>2</sub> to generate  $\bullet\text{O}_2^-$  (ref. <sup>46</sup>), which then transforms to  $\bullet\text{OH}$  radicals<sup>50</sup> and consequently degrade RhB (Fig. 4d). Indeed, the gradual generation of  $\bullet\text{OH}$  radicals during the photocatalytic process was confirmed by monitoring the formation of hydroxyl radicals over the visible light irradiation period of 40 min by PL spectroscopy (Supplementary Fig. 18).

## Discussion

In summary, we report edge-selective functionalization of BP nanosheets by covalently bonding stable C<sub>60</sub> molecules, leading to significant stability improvement of BP owing to the sacrificial C<sub>60</sub> shield. The edge-selective bonding of C<sub>60</sub> molecules via covalent P-C bonds was accomplished via a one-step ball-milling of the BP and C<sub>60</sub> mixture without any additive, thus being very facile and eco-friendly. Owing to the high stability of the hydrophobic C<sub>60</sub> molecules against light, oxygen, and water, C<sub>60</sub> effectively protects BP nanosheets from oxidation, thus significantly improves the stability of BP nanosheets in water with the degradation rate inhibited by a factor of 4.6. The involvement of C<sub>60</sub> leads to the photoinduced electron transfer from BP to C<sub>60</sub> within the BP-C<sub>60</sub> hybrid, which can inhibit the recombination of charge carriers and consequently enhance not only the photoelectric conversion property but also the photocatalytic activity of BP. Our conceptual breakthrough on selectively passivating the reactive edge sites of BP nanosheets by sacrificial C<sub>60</sub> molecules paves the way towards ambient processing and applications of BP.

## Methods

**Preparation of the BP-C<sub>60</sub> hybrid.** Bulk BP was synthesized by a phase transformation reaction from red phosphorus following a similar method reported in literature<sup>35</sup>. The BP-C<sub>60</sub> hybrid was synthesized in a planetary ball-milling machine. Typically, a mixture of 300 mg bulk BP powder and 600 mg C<sub>60</sub> powder was put into a ZrO<sub>2</sub> ball-milling jar containing 50 g ZrO<sub>2</sub> balls (3 mm diameter). The jar was sealed in a glovebox filled with Ar and finally equipped on the planetary ball-milling machine. The ball-milling process was performed at ambient temperature for total 24 h (with 15 min interval for every 30 min milling time) with the rotation speed of 250 rpm. After ball-milling, the resultant mixture was collected and Soxhlet-extracted with CS<sub>2</sub> for 48 h to remove the unreacted C<sub>60</sub>. Finally, the sample was vacuum dried for 1 day at 40 °C.

The control sample BP-BM was prepared by ball-milling a mixture of 270 mg bulk BP powder and 630 mg anhydrous LiOH powder for 12 h with 50 g ZrO<sub>2</sub> (3 mm diameter)<sup>6</sup>. C<sub>60</sub>-BM was synthesized by ball-milling pristine 1 g C<sub>60</sub> powder for 12 h with 50 g ZrO<sub>2</sub> (3 mm diameter), followed by Soxhlet-extraction with CS<sub>2</sub> for 48 h to remove the unreacted C<sub>60</sub>. The BP/C<sub>60</sub> mixture was prepared through stirring the BP-BM powders (70 wt%) and C<sub>60</sub> powders (30 wt%) in the 10 mL isopropanol solution by 24 h and removing solvent by centrifugation.

**Stability measurements.** The BP-C<sub>60</sub> and BP-BM powders were dispersed in water and sonicated for 30 min, followed by 20 min centrifugation at 9000 rpm to get dispersed BP-C<sub>60</sub> and BP-BM nanosheets aqueous solution. The BP-C<sub>60</sub> and BP-BM nanosheet aqueous solutions were kept under ambient condition for different periods, and the optical absorbance at each time point was monitored so as to investigate their stability according to the change of the optical absorbance intensity.

**Photoelectrochemical measurements.** The sample (15 mg) was dispersed in ethanol (300  $\mu\text{L}$ ), ultrasonicated for 30 min to form a homogenous ink. A volume of 100  $\mu\text{L}$  of the ink was dropped onto the conductive side of FTO slide (1 cm  $\times$  2 cm) coating  $\sim 1 \text{ cm}^2$ , followed by vacuum drying. The films on FTO were used as working electrode. The electrochemical experiments were carried out on an electrochemical workstation (CHI 660C, Shanghai ChenHua Instrument Company, China). With a typical three-electrode cell under the ambient condition and a 300 W xenon lamp (Lansheng Electronic Co., China) as light source. The counter electrode and reference electrode were a platinum wire and a silver wire. The electrolyte was 0.1 M KCl aqueous solution.

**Photocatalytic measurements.** A 5 mg sample was placed in 50 mL 0.01 mg mL<sup>-1</sup> RhB solution in a 50 mL beaker. The solution was magnetically stirred in dark for 60 min to ensure the establishment of an adsorption/desorption equilibrium between the photocatalyst and organic pollutants. Photocatalytic degradation of RhB by the powder samples under visible light irradiation was performed using a 300 W xenon lamp with a UV cutoff filter ( $\lambda > 420 \text{ nm}$ ) as light. Before irradiation, 2 mL solution was collected and tested by using UV-vis-NIR spectrometer to measure the concentration of the solution after adsorption/desorption equilibrium. During irradiation, about 2 mL solution was collected and tested by using UV-vis-NIR spectrometer every 10 min. The concentration of RhB was measured according to the absorbance at 550 nm.

To detect the formation of hydroxyl radicals, 5 mg BP-C<sub>60</sub> hybrid powder was placed in 50 mL terephthalic acid solution containing ( $4 \times 10^{-4} \text{ M}$  terephthalic acid and  $2 \times 10^{-3} \text{ M}$  NaOH). The solution was irradiated by a 300 W halogen lamp (with a 400 nm filter). At every 10 min, 1.5 mL suspensions were collected and



centrifuged. The resulted supernatants were subjected to PL measurements to detect the fluorescence spectra of the generated 2-hydroxyterephthalic acid.

**Characterization.** FTIR spectra were performed on a TENSOR 27 spectrometer (Bruker, Germany) at room temperature. The Raman spectra were obtained at room temperature with an in Via Raman Microscope equipment (Renishaw, England) with a 532 nm excitation laser. Solid-state  $^{13}\text{C}$  nuclear magnetic resonance (NMR) spectra was carried out on a AVANCE AV400 magic angle spinning (MAS) measurements (Bruker, Germany) using a standard Bruker 4 mm MAS probe with spinning speed 14 kHz. SEM images were obtained from a JEOL JSM-6390LA instrument (Rigaku, Japan). The high-resolution transmission electron microscopy (HRTEM) was conducted on a JEOL-2010 (Rigaku, Japan) microscope operating at a voltage of 200 kV. The scanning transmission electron microscopy-energy dispersive X-ray (STEM-EDX) mapping images were obtained on a JEOL-2100F (Rigaku, Japan) microscope operating at a voltage of 200 kV. X-ray photoelectron spectroscopy (XPS) was conducted on a Thermo-VV ESCALAB 250 (Thermo-VV Scientific) machine. Atomic force microscopy (AFM) measurements were carried out on a XE7 scanning probe microscope (Park, Korea). XRD patterns were obtained from a Smart Lab 9 kW X-ray diffraction instrument (Rigaku, Japan). Thermal gravimetric analysis (TGA) analysis was carried out on a Q600 SDT instrument (TA, USA) under  $\text{N}_2$  atmosphere. UV-vis-NIR diffuse reflection spectroscopy (DRS) was performed on a 3700 UV-vis spectrometer (Shimadzu, Japan). The Carbon K-edge X-ray absorption spectroscopy (XAS) and phosphorus  $L_{2,3}$ -edge XAS were collected with a 0.1 eV energy resolution at beamline 12B- $\alpha$  of the National Synchrotron Light Source (Hefei, China) at National Synchrotron Radiation Laboratory. The Phosphorus K-edge XAS were collected at beamline 16A1 of the National Synchrotron Radiation Research Center (Hsinchu, Taiwan, China). Synchrotron radiation photoemission spectroscopy (SR-PES) experiments were performed at the Catalysis and Surface Science endstation in the National Synchrotron Radiation Laboratory (NSRL), Hefei, and measured using synchrotron radiation light as the excitation source with a photon energy of 39.9 eV. A sample bias of  $-5$  V was applied to observe the secondary electron cutoff. The fluorescence spectra were measured on a Hitachi F-4500 fluorescence spectrophotometer with an excitation wavelength of 320 nm. The steady-state photoluminescence (PL) spectra were measured using an fluorescence spectrometer (Jobin Yvon, France) with an excitation wavelength of 450 nm.

## Data availability

All data supporting the findings of this study are available from the corresponding author on request.

Received: 28 February 2018 Accepted: 31 August 2018

Published online: 09 October 2018

## References

- Mannix, A. J., Kiraly, B., Hersam, M. C. & Guisinger, N. P. Synthesis and chemistry of elemental 2D materials. *Nat. Rev. Chem.* **1**, 0014 (2017).
- Li, L. et al. Black phosphorus field-effect transistors. *Nat. Nanotech.* **9**, 372–377 (2014).
- Xia, F., Wang, H. & Jia, Y. Rediscovering black phosphorus as an anisotropic layered material for optoelectronics and electronics. *Nat. Commun.* **5**, 4458 (2014).
- Batmunkh, M., Bat-Erdene, M. & Shapter, J. G. Phosphorene and phosphorene-based materials—prospects for future applications. *Adv. Mater.* **28**, 8586–8617 (2016).
- Lin, S. et al. Solution-processable ultrathin black phosphorus as an effective electron transport layer in organic photovoltaics. *Adv. Funct. Mater.* **26**, 864–871 (2016).
- Zhu, X. et al. Black phosphorus revisited: a missing metal-free elemental photocatalyst for visible light hydrogen evolution. *Adv. Mater.* **29**, 1605776 (2017).
- Walia, S. et al. Defining the role of humidity in the ambient degradation of few-layer black phosphorus. *2D Mater.* **4**, 015025–015032 (2016).
- Favron, A. et al. Photooxidation and quantum confinement effects in exfoliated black phosphorus. *Nat. Mater.* **14**, 826–832 (2015).
- Huang, Y. et al. Interaction of black phosphorus with oxygen and water. *Chem. Mater.* **28**, 8330–8339 (2016).
- Kuntz, K. L. et al. Control of surface and edge oxidation on phosphorene. *ACS Appl. Mater. Interfaces* **9**, 9126–9135 (2017).
- Liu, H., Du, Y., Deng, Y. & Ye, P. D. Semiconducting black phosphorus: synthesis, transport properties and electronic applications. *Chem. Soc. Rev.* **44**, 2732–2743 (2015).
- Kim, J. et al. Long-term stability study of graphene-passivated black phosphorus under air exposure. *Curr. Appl. Phys.* **16**, 165–169 (2016).
- Wan, B. et al. Enhanced stability of black phosphorus field-effect transistors with  $\text{SiO}_2$  passivation. *Nanotechnology* **26**, 435702–435707 (2015).
- Yang, B. et al. Te-doped black phosphorus field-effect transistors. *Adv. Mater.* **28**, 9408–9415 (2016).
- Sun, J. et al. Formation of stable phosphorus–carbon bond for enhanced performance in black phosphorus nanoparticle–graphite composite battery anodes. *Nano Lett.* **14**, 4573–4580 (2014).
- Zhang, Y. et al. An air-stable densely packed phosphorene–graphene composite toward advanced lithium storage properties. *Adv. Energy Mater.* **6**, 1600453 (2016).
- Sun, J. et al. A phosphorene–graphene hybrid material as a high-capacity anode for sodium-ion batteries. *Nat. Nanotech.* **10**, 980–985 (2015).
- Lei, W., Liu, G., Zhang, J. & Liu, M. Black phosphorus nanostructures: recent advances in hybridization, doping and functionalization. *Chem. Soc. Rev.* **46**, 3492–3509 (2017).
- Ryder, C. R. et al. Covalent functionalization and passivation of exfoliated black phosphorus via aryl diazonium chemistry. *Nat. Chem.* **8**, 597–602 (2016).
- Zhao, Y. et al. Surface coordination of black phosphorus for robust air and water stability. *Angew. Chem. Int. Ed.* **128**, 5003–5007 (2016).
- Abellán, G. et al. Noncovalent functionalization of black phosphorus. *Angew. Chem. Int. Ed.* **128**, 14777–14782 (2016).
- Tao, W. et al. Black phosphorus nanosheets as a robust delivery platform for cancer theranostics. *Adv. Mater.* **29**, 1603276 (2017).
- Zhao, Y. et al. Passivation of black phosphorus via self-assembled organic monolayers by van der Waals epitaxy. *Adv. Mater.* **29**, 1603990 (2017).
- Kadish, K. M. & Ruoff, R. S. *Fullerenes: Chemistry, Physics, and Technology* (John Wiley, New York, 2000).
- Liu, F. P. & Yang, S. F. Carbon: Fullerene in *Encyclopedia of Inorganic and Bioinorganic Chemistry* (eds Lukehart, C. M. & Scott, R. A.) (John Wiley & Sons, Chichester, UK, 2014).
- Scanlon, J. C., Brown, J. M. & Ebert, L. B. Oxidative stability of fullerenes. *J. Phys. Chem.* **98**, 3921–3923 (1994).
- Deguchi, S., Alargova, R. G. & Tsujii, K. Stable dispersions of fullerenes,  $\text{C}_{60}$  and  $\text{C}_{70}$ , in water. Preparation and characterization. *Langmuir* **17**, 6013–6017 (2001).
- Bühl, M. & Hirsch, A. Spherical aromaticity of fullerenes. *Chem. Rev.* **101**, 1153–1184 (2001).
- Popov, A. A., Yang, S. F. & Dunsch, L. Endohedral fullerenes. *Chem. Rev.* **113**, 5989–6113 (2013).
- Cui, C. H., Li, Y. W. & Li, Y. F. Fullerene derivatives for the applications as acceptor and cathode buffer layer materials for organic and perovskite solar cells. *Adv. Energy Mater.* **7**, 1601251 (2016).
- Chen, X. et al. A facile mechanochemical route to a covalently bonded graphitic carbon nitride ( $\text{g-C}_3\text{N}_4$ ) and fullerene hybrid toward enhanced visible light photocatalytic hydrogen. *Nanoscale* **9**, 5615–5623 (2017).
- Jeon, I.-Y. et al. Large-scale production of edge-selectively functionalized graphene nanoplatelets via ball milling and their use as metal-free electrocatalysts for oxygen reduction reaction. *J. Am. Chem. Soc.* **135**, 1386–1393 (2012).
- Zhu, S.-E., Li, F. & Wang, G.-W. Mechanochemistry of fullerenes and related materials. *Chem. Soc. Rev.* **42**, 7535–7570 (2013).
- Guan, J. et al. Directly bonded hybrid of graphene nanoplatelets and fullerene: facile solid-state mechanochemical synthesis and application as carbon-based electrocatalyst for oxygen reduction reaction. *J. Mater. Chem. A* **3**, 4139–4146 (2015).
- Nilges, T., Kersting, M. & Pfeifer, T. A fast low-pressure transport route to large black phosphorus single crystals. *J. Solid State Chem.* **181**, 1707–1711 (2008).
- Puziy, A. M. et al. Surface chemistry of phosphorus-containing carbons of lignocellulosic origin. *Carbon* **43**, 2857–2868 (2005).
- Hu, H. et al. Covalent functionalization of black phosphorus nanoflakes by carbon free radicals for durable air and water stability. *Nanoscale* **10**, 5834–5839 (2018).
- Sugai, S., Ueda, T. & Murase, K. Pressure dependence of the lattice vibration in the orthorhombic and rhombohedral structures of black phosphorus. *J. Phys. Soc. Jpn.* **50**, 3356–3361 (1981).
- Kuzmany, H., Matus, M., Burger, B. & Winter, J. Raman scattering in  $\text{C}_{60}$  fullerenes and fullerides. *Adv. Mater.* **6**, 731–745 (1994).
- Rouff, A. A., Rabe, S., Nachttegaal, M. & Vogel, F. X-ray absorption fine structure study of the effect of protonation on disorder and multiple scattering in phosphate solutions and solids. *J. Phys. Chem. A* **113**, 6895–6903 (2009).
- Huang, T. et al. Direct self-focusing synthesis of monodisperse  $[\text{Au}_8(\text{PPh}_3)_7]^2+$  nanoclusters. *Dalton Trans.* **46**, 12239–12244 (2017).
- Kruse, J. et al. Phosphorus  $L_{2,3}$ -edge XANES: overview of reference compounds. *J. Synchrotron Radiat.* **16**, 247–259 (2009).
- Jürgensen, A. The P (1s) and P (2p) XAFS spectra of elemental phosphorus, theory and experiment. *Phys. Scr.* **T115**, 548–551 (2005).



44. Nicotra, G. et al. Absorption edges of black phosphorus: a comparative analysis. *Phys. Status Solidi B* **253**, 2509–2514 (2016).
45. Tian, B. et al. Supported black phosphorus nanosheets as hydrogen-evolving photocatalyst achieving 5.4% energy conversion efficiency at 353 K. *Nat. Commun.* **9**, 1397 (2018).
46. Wang, H. et al. Ultrathin black phosphorus nanosheets for efficient singlet oxygen generation. *J. Am. Chem. Soc.* **137**, 11376–11382 (2015).
47. Zhang, T. et al. Degradation chemistry and stabilization of exfoliated few-layer black phosphorus in water. *J. Am. Chem. Soc.* **140**, 7561–7567 (2018).
48. Hickey, S. G., Riley, D. J. & Tull, E. J. Photoelectrochemical studies of CdS nanoparticle modified electrodes: absorption and photocurrent investigations. *J. Phys. Chem. B* **104**, 7623–7626 (2000).
49. Ren, X. et al. Environmentally robust black phosphorus nanosheets in solution: application for self-powered photodetector. *Adv. Funct. Mater.* **27**, 1606834 (2017).
50. Chai, B., Liao, X., Song, F. & Zhou, H. Fullerene modified C<sub>3</sub>N<sub>4</sub> composites with enhanced photocatalytic activity under visible light irradiation. *Dalton Trans.* **43**, 982–989 (2014).

## Acknowledgements

We are grateful to Dr. Huanxin Ju and Professor Hualing Zeng (University of Science and Technology of China) for technical assistances in SR-PES and TRPL measurements, respectively. We also thank Professor Yi Luo (University of Science and Technology of China) for stimulating discussions. This work was partially supported by the National Key Research and Development Program of China (2017YFA0402800), National Natural Science Foundation of China (Nos. 21371164, 51572254, 51672262, 51772285, and 11435012), the Major/Innovative Program of Development Foundation of Hefei Center for Physical Science and Technology (No. 2016FXZY003), and the Fundamental Research Funds for the Central Universities (WK3430000003, and WK3430000023).

## Author contributions

S.Y. conceived and designed this research. X.Z. synthesized the BP-C<sub>60</sub> samples, conducted characterizations and photoelectrochemical measurements. T.Z. prepared the

bulk BP samples. D.J. and Z.S. helped with photocatalytic measurements. H.D., H.C.J., and W.Y. carried out XAS studies. M.Z., R.G., Y.L., and M.C. helped with the material synthesis and characterizations. H.X.J., P.D., S.W., Y.L., and S.Y. co-wrote the paper, and all the authors commented on it.

## Additional information

**Supplementary Information** accompanies this paper at <https://doi.org/10.1038/s41467-018-06437-1>.

**Competing interests:** The authors declare no competing interests.

**Reprints and permission** information is available online at <http://npg.nature.com/reprintsandpermissions/>

**Publisher's note:** Springer Nature remains neutral with regard to jurisdictional claims in published maps and institutional affiliations.



**Open Access** This article is licensed under a Creative Commons Attribution 4.0 International License, which permits use, sharing, adaptation, distribution and reproduction in any medium or format, as long as you give appropriate credit to the original author(s) and the source, provide a link to the Creative Commons license, and indicate if changes were made. The images or other third party material in this article are included in the article's Creative Commons license, unless indicated otherwise in a credit line to the material. If material is not included in the article's Creative Commons license and your intended use is not permitted by statutory regulation or exceeds the permitted use, you will need to obtain permission directly from the copyright holder. To view a copy of this license, visit <http://creativecommons.org/licenses/by/4.0/>.

© The Author(s) 2018